Analysis & development of automated system for on-wafer channel thermal measurement of RF power devices using ordinary lab instruments

Analysis & Development of Automated System for On-Wafer Channel Thermal Measurement of RF Power Devices Using Ordinary Lab Instruments

1 Anwar Ali, Haider Ali, Marco Pirola, Jijun Tong

***Abstract*— Accurate and precise measurement of channel temperature for RF devices and especially for high power density devices such as MESFETs and GaAs High Electron Mobility Transistors (HEMTs) is essential for understanding the physics behind device degradation. In high power density devices, self-heating effects (SHEs) and channel to base plate temperature gradients are very high. This paper proposes an automated experimental setup using ordinary lab instruments for the measurement of channel temperature of MESFETs and HEMTs in terms of thermal resistance (θ_{th}) and thermal capacitance (C_{th}). The automated experimental setups utilize ordinary lab equipment instead of using specialized high-end tools. With ambient temperature, DC bias conditions, and RF power levels, channel temperature is calculated using θ_{th} and C_{th} parameters. The proposed technique is applied on three different HEMTs and the results were similar for all of them which reflect accuracy of the technique.**

***Index Terms*—Channel temperature, HEMT, self-heating effect, thermal resistance, thermal capacitance.**

I. INTRODUCTION

ACCURATE channel temperature measurement is significantly important in high power devices such as GaAs HEMTs because of their self-heating and high channel to base plate temperature gradients [1], [2] [3], 4]. The lifetime and performance of RF devices decrease with increase in channel temperature. When power is applied to the transistor for certain time, its channel temperature tends to increase. This increase of channel temperature affects the device performance and is called self-heating effect (SHE) [5], [6] which can be characterized in terms of thermal parameters such as thermal resistance (θ_{th}) and thermal capacitance (C_{th}) [7]. Through these parameters the reliability (lifetime) and mean time to failure (MTTF) of the device can be predicted [8]. This is especially true for GaAs HEMTs devices [9] which are the focus of this work.

To understand SHE in GaAs HEMT devices, the transistor is imagined as a rectangular patch on the surface of a GaAs substrate that dissipates power uniformly over its area. The thermal estimation is analogous to introducing a current on the surface of a three-dimensional network of resistors, which represents the thermal resistance of the GaAs substrate. When current (power) is injected to the device, the device heats up and voltage (temperature) develops near the channel [10]. The increase in temperature is directly proportional to the power dissipated in the channel [11]. It is highly peaked in the high field region below the gate contact close to the drain [12], but these peak points or absolute temperature measurement is not the focus of this work rather it measures the average temperature over the gate region (Channel temperature). Channel to case thermal resistance ($\theta_{th\text{-}CHC}$) is used to measure the channel temperature of a HEMT as given by (1);

(1)

Where, T_{ch} is the channel temperature ($°C$), T_c is the case or flange temperature ($°C$) and P_d is the power dissipated by the device. Thermal capacitance (C_{th}) is a measure of the capability of accumulating heat, with unit Ws/°C [12]. Thermal behavior of a device changes when dynamic phenomena are considered (pulse power operation). This behavior can be described in terms of C_{th}, which is given by (2);

(2)

Where, P is the power ΔT is the temperature difference, and t is the heat accumulation time.

The electrical analogy of the thermal behavior of an active device, package, printed circuit board, external heat sink and external ambient is a chain of RC cells represent the characteristic time constant (τ) [13]. In case of an active device that consist of wafer and contacts, will have two RC cells and thus two time constants R_1C_1 and R_2C_2 as shown in Fig. 1.

Several approaches exist for the measurement of thermal resistance (θ_{th}) and thermal capacitance (C_{th}) but the most famous measurement techniques are the delta V_{gs}, the liquid

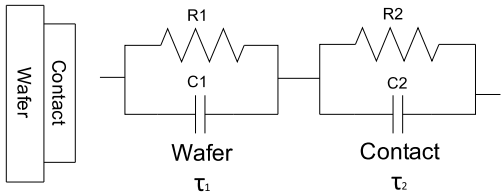

(a) (b)

29 December 2020.

Anwar Ali is Associate Professor at the School of Information Science and Technology, Zhejiang Sci-Tech University, Hangzhou, China
Haider Ali is Assistant Professor at the Department of Electronics Engineering Technology, University of Technology, Nowshera, Pakistan
Marco Pirola is full Professor at the Department of Electronics and Telecommunications (DET), Politecnico di Torino, Turino, Italy
Jijun Tong is full Professor at the School of Information Science and Technology, Zhejiang Sci-Tech University, Hangzhou, China
Corresponding author Email: haider.ali@uotnowshera.edu.pk

Fig. 1: (a) Device (b) Electro-thermal model

crystal and photocurrent spectral analysis. The liquid crystal measurement technique provides good absolute temperature accuracy and very fine spatial resolution [14]. But the problem is that the device thermal impedance is affected and secondly, it requires very expensive specialized instruments not easily available in every laboratory. The photocurrent spectral analysis technique measures directly the channel temperature, but this technique also requires specialized and expensive instrument setup [15]. Infrared thermography is commonly used for thermal imaging, is also unsuitable for thermal analysis of these devices as it has only 5–10μm lateral resolution [16]. This low resolution is not adequate to probe the micrometer-size source drain openings in RF devices. Optical thermal measurement techniques such as infrared thermal imaging and micro Raman spectroscopy [17] are frequently used for channel temperature measurement but they have many limitations. First, they require specific device geometry, i.e. large gate/drain gap and limited field plate for a direct access to the device which is difficult to measure a fully packaged device [18]. Furthermore, the experimental setup is not easily available. Finally, optical techniques measure vertically averaged temperature of the device where the precise channel temperature is difficult to measure [19]. The method employed in this paper is similar to the techniques that include [1] and [20]. These techniques are also based on pulse measurement method, but they measure only thermal resistance of the device. Secondly, the technique discussed in [1], directly apply voltage pulses to the device which can result is high current flow and can damage it [21]. While in the technique discussed in this paper, apply controlled current pulses to the device.

II. THE DELTA V_{GS} MEASUREMENT TECHNIQUE

In this paper, delta V_{gs} measurement technique is used for measuring channel thermal parameters i.e. θ_{th} and C_{th}. This technique directly measures the channel temperature and provides a quick, easily repeatable and non-destructive determination of thermal parameters. This technique utilizes the generic laboratory instruments such as oscilloscope and function generator, and does not require expensive, specialized laboratory instruments like other technique [14], [15] and [16].

The measurement setup is shown in Fig. 2(a) and Fig. 3(a), which maintains a constant forward gate current through the gate-source diode. In order to heat up the device a voltage pulse between the drain and source is applied. After each heating pulse, the drain and source are shorted with each other and a measurement of the voltage drop across the gate-source diode is performed.

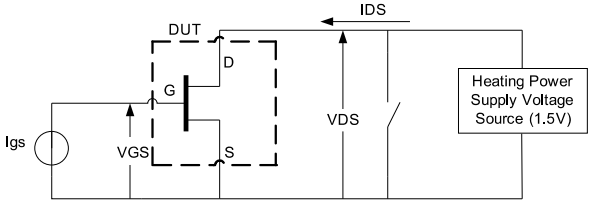

(a)

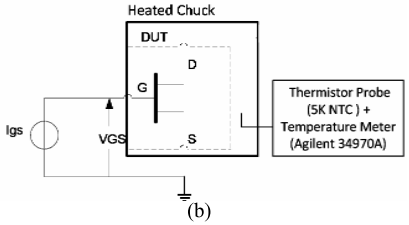

(b)

Fig. 2: (a) Simplified schematic for Delta V_{gs} measurements; (b) Simplified Thermal calibration schematic for K-factor calculation.

The *K*-factor for a device is given by (3);

(at constant current) (3)

The *K*-factor depends on the type of device which involves particular processing for that device. Here, for a device under test (DUT) placed in chuck (a temperature controlled environment), *K*-factor is calculated by varying temperatures and measuring the voltage across the forward conducting gate-source Schottky junction at constant I_g for different temperatures ranging from 23°C to 63°C. The same process is repeated for other values of I_g where V_{gs} is calculated from 23°C to 63°C. For consistency, it is important to stabilize temperature (a pause of 6 minutes is observed) before each measurement is performed.

Using measurement setup in the Fig. 2(b), the ΔT value can be found with respect to the corresponding ΔV. This helps in computing K-factor as given in Fig. 5 and Fig. 6.

If the device *K*-factor, the amount of power supplied by the heating pulse and the ΔV_{gs} measured at the time before and after the heating pulse ($\Delta V_{DS} I_{DS}$) are known, θ_{th} can be measured using (4) [18];

(4)

Where, = channel-to-case thermal resistance (°C/watt)
= change in voltage across gate-source diode (from time before to after heating pulse)
= Drain-source heating pulse voltage
= Drain-source heating pulse current

Thermal resistance generally increases with increase in temperature. This is due to decrease in thermal conductivity as channel temperature of GaAs increases [22]. Beyond certain channel temperature (270˚C [23]), thermal conductivity increases and results in lower thermal resistance. The reduction in thermal resistance is due to the leakage current flowing through the substrate and buffer layer.

III.EXPERIMENTAL WORKBENCH SETUP

In order to carry out any sort of analysis or characterization of a circuit or device, it is necessary to build up the right setup that can provide the desired results with the required accuracy. Fig. 3 depicts the experimental setup and DUT. For better understanding, the basic block diagram on the bench physical connectivity is shown in Fig. 4. The automatic measuring system for the characterization of pulsed RF transistor comprises of the following ordinary laboratory instrumentation:

- 4-channels oscilloscope (DSO6034A)

- Signal generator (HP33220A)
- Programmable DC power supply (HP6624A)
- Current buffer

A. Thermal Calibration and K-Factor Measurement

Using the measurement setup shown in Fig. 3(a), V_g vs. I_g characterization is performed at 23°C for the GaAs HEMT device shown in Fig. 3(b). It is clear from the temperature calibration curves shown in Fig. 5 that the Schottky barrier acts as a characteristic forward diode junction. In the same manner the V_g vs. I_g curve for different temperatures ranges (23°C to 63°C) are measured. In HEMTs, the K-factor calibrations should be done in linear region to avoid self-heating effect which can cause inconformity of ambient and channel temperature [24].

(a) (b)

Fig. 3: Photo of (a) experimental bench setup (b) GaAs HEMT (POW1B) device

Fig. 5 shows that the threshold voltage V_T decreases with increase in device temperature. Fig. 5 depicts that the variation of V_g vs. I_g curves, while Fig. 6 represents the evaluated K-factor model which shows insignificant variation of 0.0028 (-0.7635 to -0.7605) that yields an average value of K = -0.7620.

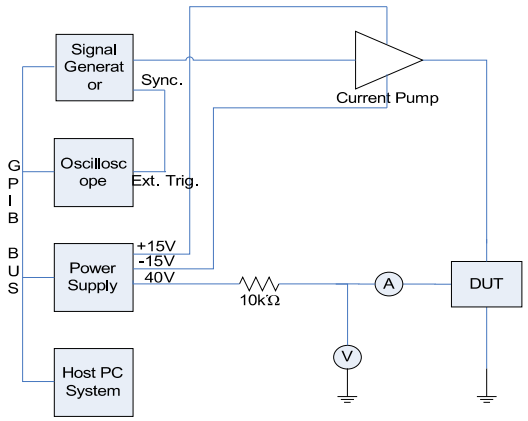

Fig. 4: Basic block diagram of experimental physical bench connectivity.

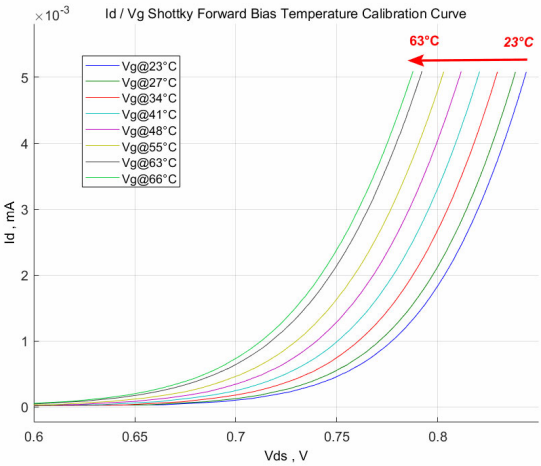

Fig. 5: I_g vs. V_g Schottky forward bias junction temperature calibration curve

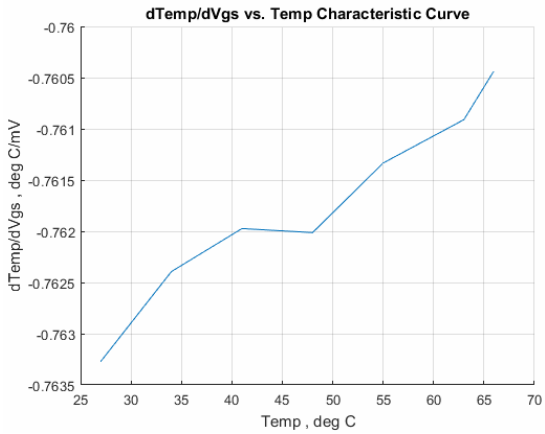

Fig. 6: Computed K-factor variation vs. temperature change

After the computation of *K*-factor, the thermal resistance (θ_{th}) can be found through Pulsed Drain Measurements (PDM) technique. The proceeding section deals with the theoretical aspect and the procedure behind PDM.

B. Pulsed Drain Measurements

In PDM a rectangular pulsed signal is sent via drain to heat up the transistor channel. At the same time the gate is kept at a constant current. Care should be taken that the drain pulse duration should be long enough with respect to the thermal time constant unless the thermal capacitance is shorting the thermal pulse. Basic block diagram of the PDM experimental bench connectivity is shown in Fig. 4.

The PDM procedure can be divided into following steps.

1. Connect a 4mA current source to the gate terminal of DUT: As with the available Power Supply (HP-6624A) per channel output voltage is 20V. Two output channels are connected in series to get 40V. A 10KΩ series resistor is added to generate constant current source of I_g = 4mA.
2. Pulse signal is generated by a waveform generator and is amplified by a current buffer which in actual is a current feedback amplifier, designed using LT1210 [25], having a fixed gain of 3.7 (to stabilize speed and slew rate

bandwidth), maximum current rating of 1.1A and a series resistance of 10Ω is added for DUT stability and protection against burnout. The polarity of the current pump is maintained to allow dual characterization for both n-channel and p-channel devices. It is done by having a fixed (non-varying) feedback resistance R_f in the feedback current amplifier to avoid oscillations. Having a varying R_f halves the RF Bandwidth at maximum gain.

3. The measurement equipment of the automated bench are interconnected through a GPIB bus to a host computer.

In the measurement setup a pulsed signal is applied for a specific time and then removed which heats up the channel. The device is allowed to cool down. Here it is significant to observe that the cooling happens steadily. Hence the dynamics associated with thermal capacitance of the channel is not a high frequency component. Furthermore, this method considers the overall response of the channel and does not account for microscopic details such as hotspot appearing at gate fingers level or thermal profile along the channel. Also, the data acquisition performed has its own limitations which need to be considered such as LSB quantization errors, oscilloscope probes parasitic, etc., which tends to cause high frequency noise components. Proceeding section discusses the measurement bench optimization techniques to minimize all these errors.

IV. MEASUREMENT RESULTS FOR HEMT-DUT

The PDM measurements were done on the device POW1B (fabricated by Nitronics Ltd., [26]) with 1mm1mm dimensions and maximum power rating, P_{MAX} = 1W. The measurement steps given in section III (B) were followed using the experimental setup of Fig. 3 (b) and block diagram of Fig. 4. The feed probe used is a GSG (ground-signal-ground) with a pitch of 200µm for direct measurement of the on wafer DUT. A pulse was applied on the drain terminal with amplitude V_A=12V, duty cycle D = 50%, and time period T = 50ms. The results for each measured parameter i.e. V_{ds}, V_{gs}, and I_d are plotted in Fig. 7 (a), (b) and (c) respectively. These results reveal overshoots and distortions in the measurement, caused by the parasitic of the test bench apparatus. There are significant impacts of the parasitic inductances and capacitances of the interconnects (like cables and oscilloscope probes except GPIB bus). Moreover, as compared to parasitic capacitances, the inductances play major role in distorting the signal and increasing overall signals delay which are directly proportional with interconnects length [27].

A. Interconnect Optimization

In order to minimize the interconnect effect on the measurements and to acquire precise and accurate measurements, the following modifications were done;

1. Shorter generator cable
2. Special oscilloscope probes
3. Shorter generator cable plus oscilloscope probes

Using shorter generator cables, current pump feeding cables and special oscilloscope probes (by removing probe tip and ground lead wire and replacing it with a setup similar to ground spring), the overall parasitic inductances are significantly minimized [27]. The measurement results of the modified three cases along with coaxial cable are shown for comparison in Fig. 7 (d), (e) and (f). A shift in the signal amplitude and time can be seen in all the three cases. The amplitude variation is due to comparatively higher potential drop in oscilloscope probe as compared to coaxial cable. The time shift is due to the fact that shorter generator cable has less propagation delay in comparison with longer generator cable.

The focus is not on such systematic differences and therefore can be neglected. On the other hand, distortions, undershoots, oscillations, ringing, and oscilloscope least significant bit (*LSB*) quantization error noise cannot be overlooked. In fact, the comparison is going to be based on all these parameters and the optimum case which is suitable for the measurements will be selected. Some parameters were considered for comparison of different interconnect modifications.

These parameters are as under:

- Transient time (ΔT)
- Maximum transient oscillation (Overshoot)
- Minimum transient oscillation (Undershoot)
- *LSB* Quantization error noise

It can be inferred from table 1, the optimum case is using oscilloscope probe which presents relatively better performance and results. Therefore, all proceeding measurements will include this test bench configuration.

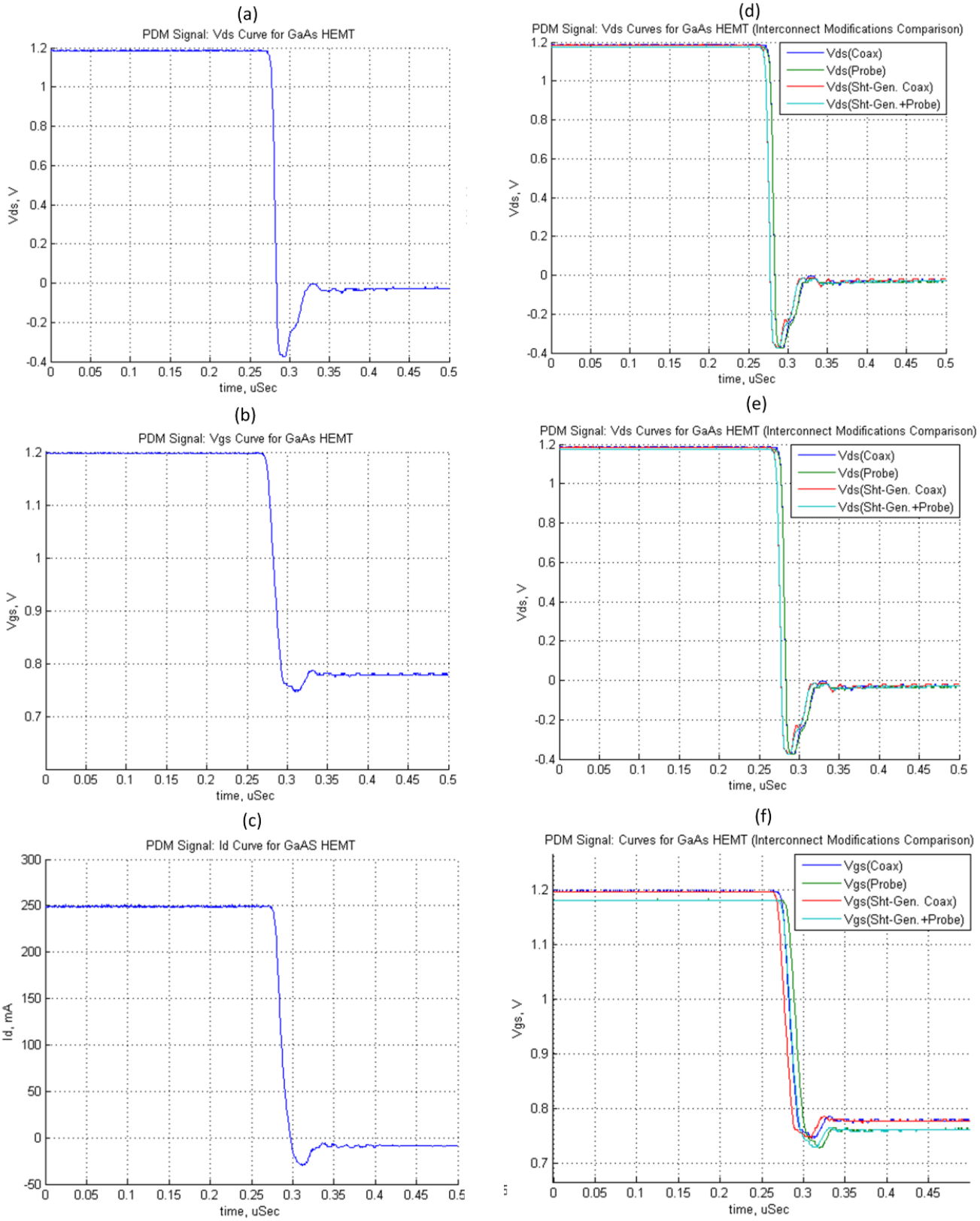

Fig. 7: PDM Signal: (a)V_{ds}, (b) V_{gs}, (c) I_d and (d) V_{ds}, (e) V_{gs} (f) I_d curves with different interconnects comparisons for GaAS HEMT (POW1B)

V. POST-PROCESSING FOR THERMAL RESISTANCE & THERMAL CAPACITANCE EXTRACTION

So far, the test-bench was optimized to get the desired measurement results required in θ_{th} and C_{th} extraction. This section discusses the post-processing procedure that is employed for the extraction of θ_{th} and C_{th}.

A. Thermal Resistance (θ_{th}) Extraction

The θ_{th} extraction is performed for three different HEMT devices on the same GaAs wafer. These devices are POW1, POW1B and POW1G, which have similar structures with minor variations that can be neglected (i.e all have same number of gate fingers and finger spacing).

θ_{th} is a temperature dependent parameter which is related to the steady state response of the system and is not dependent on transient behavior.

θ_{th} extraction procedure can be divided into two main stages:

1. De-embedding R_SI_D
2. θ_{th} calculation

TABLE I
PARAMETERS COMPARISON FOR SELECTING THE OPTIMUM INTERCONNECT CASE

Interconnects Modification		ΔT (µs)	Max. Osc. Over-shoot	Min. Osc. Under-shoot	Max. Value	LSB Quant. Error Noise
Co-axial	Vds(V)	0.2037	-0.0135	-0.3722	1.183	High
	Vgs(V)	0.1677	-0.004656	-0.0287	0.25	High
	Id(mA)	0.2573	-0.006844	-0.03	0.2511	High
Shorter Gen. Co-axial	Vds(V)	0.2122	-0.0128	-0.3722	1.183	High
	Vgs(V)	0.1401	0.7875	0.7469	1.1969	High
	Id(mA)	0.2573	-0.006844	-0.03	0.2511	High
Probe	V_{ds}(V)	0.1827	-0.0128	-0.3722	1.175	Low
	V_{gs}(V)	0.0806	0.7656	0.7281	1.1844	Low
	I_d(mA)	0.2573	-0.002781	-0.0289	0.2508	Low
Probe+ Shorter Gen. Co-axial	V_{ds}(V)	0.2122	-0.0128	-0.3722	1.175	Med.
	V_{gs}(V)	0.1066	0.7656	0.7312	1.1812	Med.
	I_d(mA)	0.1677	-0.004656	-0.0287	0.25	Med.

1) De-Embedding R_SI_D

The V_{gs} signal depicted in Fig. 7, is not truly V_{gs} as it has an embedded source resistance R_S term as given in (5);

(5)

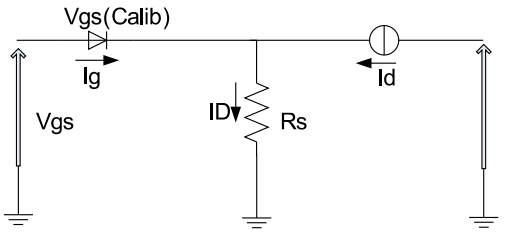

Fig. 8: Equivalent circuit diagram of actual Schottky Junction in GaAs HEMTs

Thus, V_{gs} has an appended source voltage drop (R_SI_D) that needs to be de-embedded to obtain $V_{gs(de\text{-}embed)}$. Fig. 8 gives a circuit level description of the scenario. $V_{gs(Calib)}$ =0.8187V (the forward voltage diode drop for POW1B) can be inferred from the thermal calibration procedure by keeping constant Ig=4mA at 23°C (as shown in Fig. 5). The Rs has almost negligible impact on the $V_{gs(Calib)}$ as I_d = 0 during temperature calibration process.

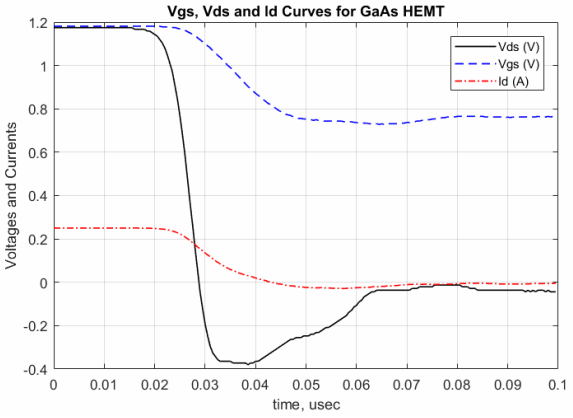

Fig. 9: V_{gs}, V_{ds} and I_d curves for GaAs HEMT before de-embedding.

From Fig. 9, $V_{gs(max)}$ = 1.181V, I_d = 250 mA and I_g = 4mA. Here, $V_{gs(Calib)}$ = 0.8187V (inferred from thermal calibration). Re-arranging equation (5) gives;

(6)

The resultant R_s is 1.426Ω from (6). To get de-embedded $V_{gs(de\text{-}embed)}$ and $V_{ds(de\text{-}embed)}$ curves, subtract R_SI_D from V_{gs} and V_{ds} curves respectively as shown in Fig. 10.

For the de-embedded values of $V_{gs(max)}$ and $V_{gs(min)}$, subtract R_SI_D term from $V_{gs(max)}$ and $V_{gs(min)}$ values given in Fig. 10. Where as, $R_SI_{D(max)}$ = (1.42637)(250x10^{-3})= 0.35659V and $R_SI_{D(min)}$ = (1.42637)(-7.6x10^{-3}) = -0.01087V. Here, $V_{gs(max)de\text{-}embed} = V_{gs(max)} - R_SI_{D(max)}$ = 1.181 – 0.35659 = 0.82441V, $V_{gs(min)de\text{-}embed} = V_{gs(min)} - R_SI_{D(min)}$ = 0.7625 – (-0.01087) = 0.77334V, $\Delta V_{gs} = V_{gs(max)de\text{-}embed} - V_{gs(min)de\text{-}embed}$ = 0.82441 – 0.77334 = 0.05107V, and ΔV_{gs} = 0.05107V.

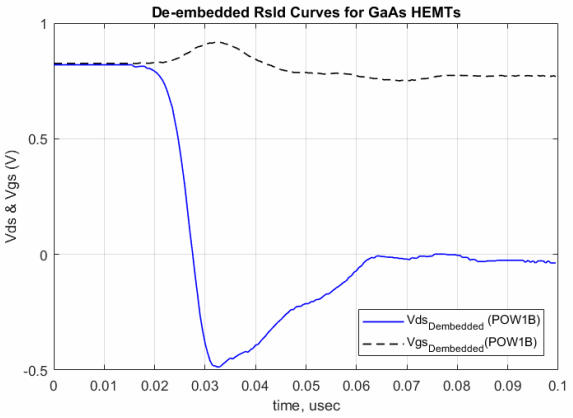

Fig. 10: De-embedded Vgs and Vds Curves

It is important to note that the difference in gate voltage behaviour during temperature calibration method and PDM is due to the fact that there is no high V_{ds} that affects V_{gs} in temperature calibration method while in the pulsed drain method PDM there is a high V_{ds} which may cause a decrease in V_{gs} as there is a constant current Ig= 4mA acting at gate [28].

2) Thermal Resistance (θ_{th}) Calculation

θ_{th} of POW1B is calculated using (4), where $\Delta T = \Delta V_{gs} K = 38.915^{\circ}C$, while $I_D V_D$ is given by (7);

(7)

Inserting values in (7), results in $I_D V_D$ = 298.32mW. By putting values in (4), gives θ_{th}= 131.924˚C/W.

The measurement process was repeated for the same device by increasing the ambient temperature step wise from 15 to 35°C and it was found that θ_{th} increased almost linearly from 125.25˚C/W to 137.75˚C/W, respectively. This shows that θ_{th} is linearly dependent on the temperature as reported in [29].

θ_{th} for the two other HEMT devices i.e. POW1 and POW1G were also extracted by performing the same post-processing procedure. Fig. 11 presents the PDM results of POW1, POW1B and POW1G.

Fig. 11 shows that all the three devices have identical V_{doi} curves because the current buffer with a gain of 3.67 is feeding equivalent input voltage i.e 1.2V to all the three devices results in an output voltage of 4.4V. Furthermore, V_{ds}, I_d and V_{gs} curves are comparatively different due to variation in power dissipation P and threshold voltages V_T (hence $V_{gs(Calib)}$ is also different).

The de-embedding is performed in the same manner as previously done in the case of POW1B. The difference here is that R_S should be separately evaluated for each device because of different $V_{gs(Calib)}$ values as R_S depends on $V_{gs(Calib)}$. Thus, $V_{gs(de-embedded)}$ and $V_{ds(de-embedded)}$ curves are different for three devices, as shown in Fig. 12.

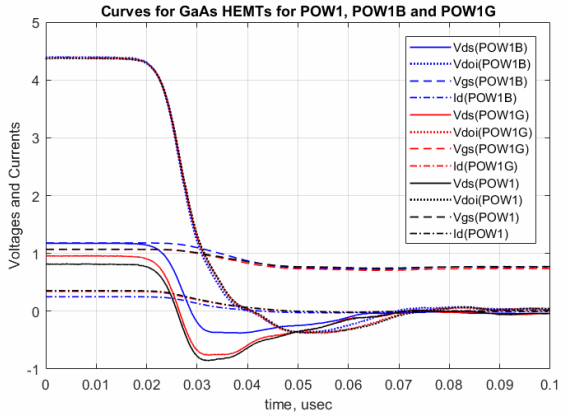

Fig. 11: PDM curves of V_{doi}, V_{ds}, I_d & V_{gs} (prior to de-embedding) for different GaAs HEMT devices (POW1, POW1B & POW1G)

Table II shows the extraction results along with certain key parameters where, the following observations can be made:

- θ_{th} is almost similar in three cases with minor variation
- ΔT varies almost linearly with respect to the power dissipated (ΔP)
- ΔV_{gs} is almost similar for all three

It can be concluded from these results that θ_{th} can be measured with considerable precision and accuracy by delta Vgs method. The agreement of θ_{th} values for the three devices verifies the repeatability of the proposed automated test-bench.

B. Thermal Capacitance (C_{th}) Extraction

During high to low (HL) transition in PDM waveforms, a sudden drop of V_{gs} and V_{ds} is experienced as shown in Fig. 11. Ideally, there should be a steep falling response of the pulsed signal. But in reality it is not true as there is a sudden change of power level in a very short time interval but the device cannot release the stored thermal energy at once. It is rather released steadily in a finite time interval. Therefore, a device which is initially heated and is in high temperature state requires a certain amount of time to cool down to a low temperature state. Thus, a steadily varying signal is observed. This steadily varying signal contains τ associated with the C_{th}. However, the behavior is not as of a lumped thermal impedance model but rather resembles that of a distributed thermal impedance model.

Once the frequency response $H(\omega)$ is evaluated, we can try to extract C_{th} from the poles of the $H(\omega)$ frequency spectrum. From signal theory, it is known that $H(\omega)$ equivalent transfer function in time domain is called impulse response $(h(t))$, given by (9);

(9)

The measured $V_{ds(de-embedded)NF}$ signal can be considered as an output of the system subjected to a rectangular pulsed input signal ($V_{ds(de-embedded)}$). This transfer function can be termed as the step response $(h_S(t))$ of the system.

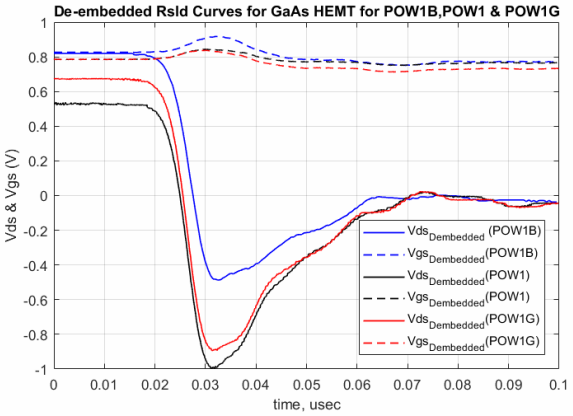

Fig. 12: PDM V_{ds}, & V_{gs} curves of for different GaAs HEMTs (POW1, POW1B & POW1G) with de-embedded $R_S I_D$

TABLE II
CALCULATIONS OF DIFFERENT PARAMETERS FOR ΘTH EXTRACTION
(* THESE VALUES ARE TAKEN AT STEADY STATE)

θ_{th} Extraction Parameters	Device's Name		
	POW1	POW1B	POW1G
$V_{gs(Calib)}$ (V)*	0.8160	0.8186	0.7800
R_S (Ω)	0.7068	1.4272	0.8572
$V_{gs(max)}$ (V)*	1.0705	1.1813	1.0771
$V_{gs(min)}$ (V)*	0.7718	0.7627	0.7312
I_D (A)	0.3561	0.250	0.3426
$V_{ds(max)de-embed}$ (V)*	0.5627	0.8178	0.6584
$V_{ds(max)de-embed}$ (V)*	-0.0244	-0.0209	-0.0298
$V_{gs(max)de-embed}$ (V)*	0.8188	0.8244	0.7834

$V_{gs(max)de\text{-}embed}$ (V)*	0.7669	0.7722	0.7251
ΔV_{gs} (V)	0.0519	0.0522	0.0584
ΔP (mW)	0.2902	0.2983	0.3264
ΔT (°C)	39.787	39.3166	44.772
θ_{th} (°C/W)	**137.120**	**131.924**	**137.1812**

The related impulse response *h(t)* of the system can be evaluated by taking the derivative of $V_{ds(de\text{-}embedded)N}$. Then, FFT is performed to evaluate *H(ω)*.

The process of obtaining a frequency response *H(ω)* can be divided into following major steps.

- Averaging & Normalization
- Differentiation
- FFT - Frequency Response

1) Averaging & Normalization of $V_{ds(de\text{-}embedded)}$

Through the test-bench, a constant current source signal with I_g=4mA is applied at gate. A steady gate voltage V_{gs} is observed when a pulse signal is applied at drain. This pulse signal causes self-heating of the channel (between drain and source of GaAs HEMT). During HL transition of the drain signal, a significant drain to source voltage drop ($\Delta V_{ds(de\text{-}embedded)}$) is experienced. Its transient analysis reveals that $\Delta V_{ds(de\text{-}embedded)}$ is relatively slow as compared to applied drain pulse. A closer analysis shows that a time constant is associated with this $V_{ds(de\text{-}embedded)}$ change and C_{th} can be extracted from a noise free $\Delta V_{ds(de\text{-}embedded)}$ signal. To acquire a noise free $V_{ds(de\text{-}embedded)}$ signal, cancellation is performed using samples averaging in both Oscilloscope and Matlab® Software. After applying different averaging ratios for both oscilloscope and Matlab® Software, the optimum trade-off value was found. Upon exceeding the optimum averaging value, the Matlab® Software averaging noise is significantly reduced but results in loss of useful part of the signal such as fast variations and fluctuations. On the contrary if oscilloscope averaging is increased from optimum value, the problem of LSB quantization error becomes significant. Thus, by repetitive trial and error method an optimum value for averaging ratios of 8 was found for both Matlab® Software and Oscilloscope, as shown in Fig. 10.

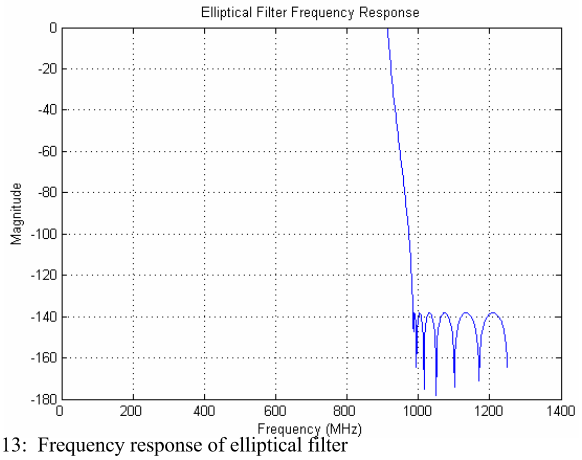

Fig. 13: Frequency response of elliptical filter

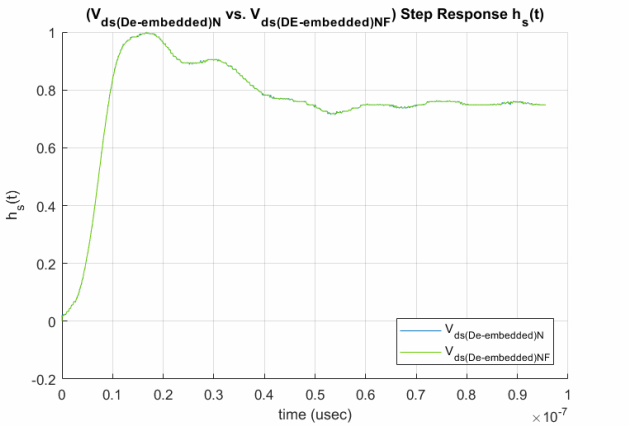

(a)

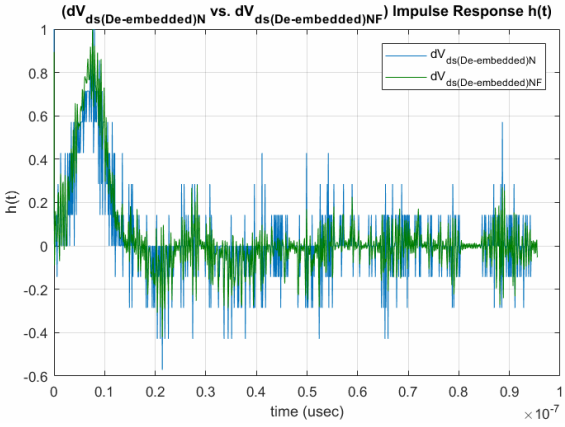

(b)

Fig. 14: (a) $V_{ds(de\text{-}embedded)N}$ & filtered $V_{ds(de\text{-}embedded)NF}$ curves (Step Reponse); (b) Differentiated $dV_{ds(de\text{-}embedded)N}$ & $dV_{ds(de\text{-}embedded)NF}$ curve (Impulse response h(t))

The V_{ds} curve is inverted and normalized with respect to maximum value $V_{ds(de\text{-}embedded)max}$, in order to represent the curve as a step response $h_s(t)$. The normalized signal ($V_{ds(de\text{-}embedded)N}$) is aligned properly on horizontal axis, to avoid any unnecessary zero terms in the beginning of $V_{ds(de\text{-}embedded)}$ which generates unwanted erroneous poles in FFT frequency domain as shown in (10) [30];

(10)

$V_{ds(de\text{-}embedded)N}$ is passed through a low-pass elliptical filter of order 'N=13', with passband and stopband frequencies of 913MHz to 986MHz respectively, as shown in Fig. 13. This filtering process eliminates any unwanted high frequency components and $V_{ds(de\text{-}embedded)NF}$ is obtained at the output of the elliptical filter.

Fig. 14(a) depicts curves for both normalized $V_{ds(de\text{-}embedded)N}$ and filtered $V_{ds(de\text{-}embedded)NF}$. From close inspection of $V_{ds(de\text{-}embedded)NF}$, it can be observed that fluctuation errors are lessened by a considerable amount in magnitude as compared with $V_{ds(de\text{-}embedded)N}$.

2) Differentiation of $V_{ds(de\text{-}embedded)NF}$

After normalization and filtering, $dV_{ds(de\text{-}embedded)NF}$ can be considered as the step response $h_S(t)$ of the system which needs to be differentiated to get the impulse response h(t) thus obtaining $dV_{ds(de\text{-}embedded)NF}$ and $dV_{ds(de\text{-}embedded)NF}$. It can be observed

that both $dV_{ds(de\text{-}embedded)N}$ and $dV_{ds(de\text{-}embedded)NF}$ resembles in shape to delta functions. There are still some short spikes due to high frequency noise components which are comparatively low in filtered $dV_{ds(de\text{-}embedded)NF}$ signal as shown in Fig. 14(b).

3) *Fast Fourier Transformation (FFT)- Frequency Response*

To acquire the frequency response, FFT algorithm is applied to the $dV_{ds(de\text{-}embedded)NF}$ data. The FFT has frequency range (f_R) from 1/(Signal length) to 1/Fs which is 10MHz to 10GHz in this case.

a) FFT Results

The FFT spectrum of $dV_{ds(de\text{-}embedded)NF}$ is given in Fig. 15(a). The spectrum has a cutoff at 100MHz. Distortion can be seen which goes on increasing above the cutoff frequency. The distortion is added up by the parasitic effects (as discussed) of the testbench and LSB quantization errors.

In order to acquire the complete transient response without errors, the FFT response shown in Fig. 15(a) should be investigated below 10MHz. For this purpose, the signal time interval is increased from 0.1µs to 2.5µs which helps to reach down to 4KHz in frequency spectrum [31].

This is achieved by modifying the testbench. Instead of acquiring samples of a single oscilloscope window interval (1000 samples), multiple oscilloscope window intervals samples are acquired by adding a time offset between consecutive window acquisitions.

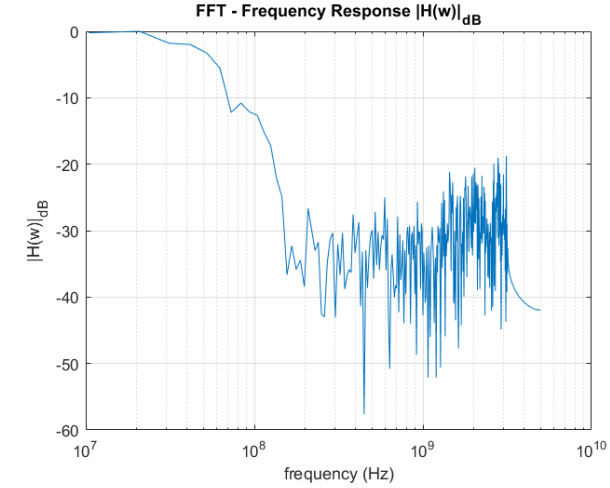

(a)

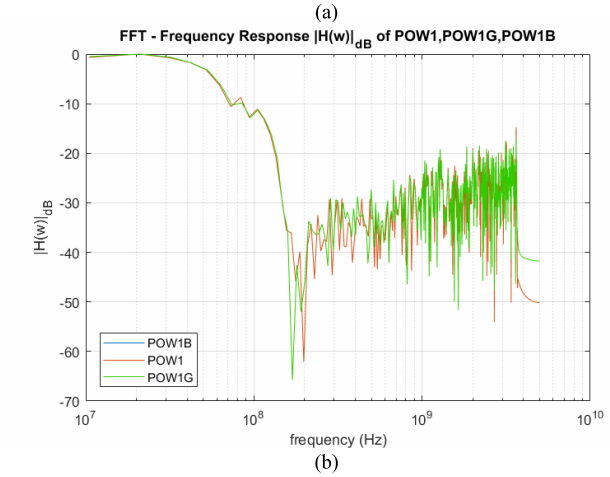

(b)

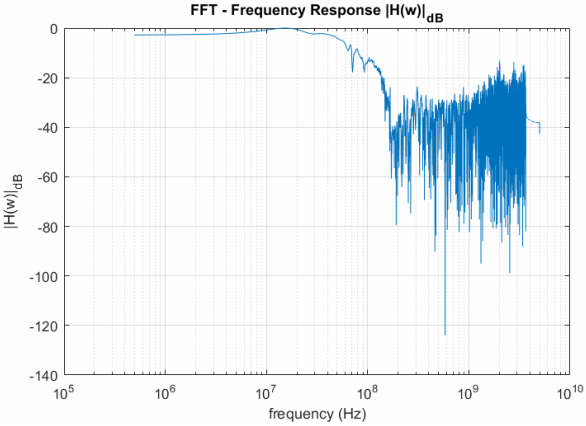

(c)

Fig. 15: (a) FFT-Frequency response H(ω); (b) Comparison of Frequency Response H(ω) for different GaAs HEMT devices; (c) FFT H(ω) for the extended time interval (21 oscilloscope frames)

Concatenation of these windows enables in acquiring samples for a longer duration as shown graphically in Fig. 16. The frequency response of Fig. 15(c) reveals a steady rise of spectrum less than 10dBs/dec from 500 kHz to 10 MHz. After 10MHz there is a sharp fall almost 20dB/dec until 30 MHz and from 30 MHz to 40 MHz the spectrum is constant with no change (0dB/dec).

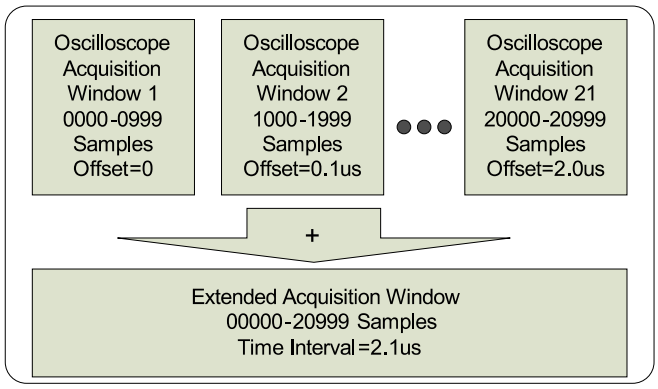

Fig. 16: Graphical representation of samples acquisition for extended time interval

Similar to Fig. 15(a) (single sample window H(ω) spectrum), there is a sharp cutoff till 100 MHz and above 100MHz distortions can be observed. The distortions are due to the parasitic effects of the testbench and LSB quantization noise. FFT for other two GaAs HEMT devices i.e. POW1 and POW1G was calculated using similar process. The FFT curves for all the three GaAs HEMT devices mounted on the same wafer reveals a similar frequency response, H(ω) behavior. It is due to the fact that that all of these devices have almost similar design layout such as gate length and gate fingers and spacing between adjacent fingers. A comparison of Frequency Response H(ω) for different GaAs HEMT devices is shown in Fig. 15(c).

b) Multirate Sample Acquisition

Further improvement is made by performing the measurement for different time scales (time/div) on oscilloscope and averaging them. This helps to keep a variable

sampling resolution; high where the signal is varying fast and low in comparatively slow varying signal range. The acquired signal has a variable time representation where FFT cannot be directly evaluated (as FFT is an LTI (Linear Time Invariant) operation). The signal is first linearized by performing interpolation between consecutive samples where the sampling interval (T_s) is selected equal to the smallest interval of the already acquired signal. This makes the time differences uniform and linearizes the signal which makes the FFT evaluation possible. Fig. 17 gives a graphical perspective of this improved acquisition process.

The acquired results of $V_{ds(de\text{-}embedded)F}$, $dV_{ds(de\text{-}embedded)NF}$ and FFT obtained through multi-rate sampling technique are shown in Fig. 18.

In comparison to previous case, $V_{ds(de\text{-}embedded)NF}$ and $d\,V_{ds(de\text{-}embedded)NF}$ shown in Fig. 18(a) and Fig. 18(b) has an improved resolution in time domain which allows to track fast changes in a better manner and therefore can provide a more accurate FFT transformation.

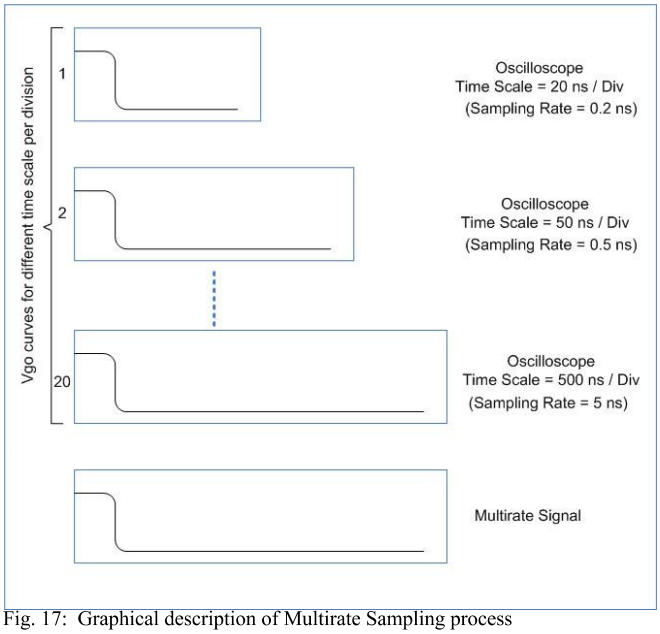

Fig. 17: Graphical description of Multirate Sampling process

The FFT-frequency response (H(ω)) computed through multi-rate sampling technique as shown in Fig. 19 has slow decaying trend of H(ω) (less than 10dB/dec) is observed from 350KHz-7MHz. It is not a lumped impedance behavior but is more complex. It can be compared to a distributed model which can be more precisely calculated by curve fitting techniques which we plan to perform in future. We can compare the above with a lumped model consisting as shown in Fig 19. The decaying trend increase considerably from 10MHz-30MHz. τ is also associated with this section of spectrum but it is suppressed due to other parasitic. Increasing trend of spectrum is observed from 10MHz-20MHz. The parasitic inductances of the test-bench are responsible for this behavior. Sharp cutoff is observed at 40MHz. Below this cutoff frequency, the system is compared to a lumped model approximated by the curve fitting. Above 100MHz we observe some distortions that show an increasing trend. These distortions are due to parasitic inductances and LSB quantization noise.

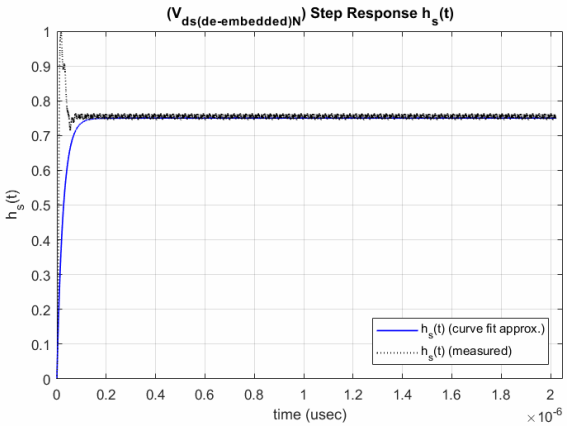

(a)

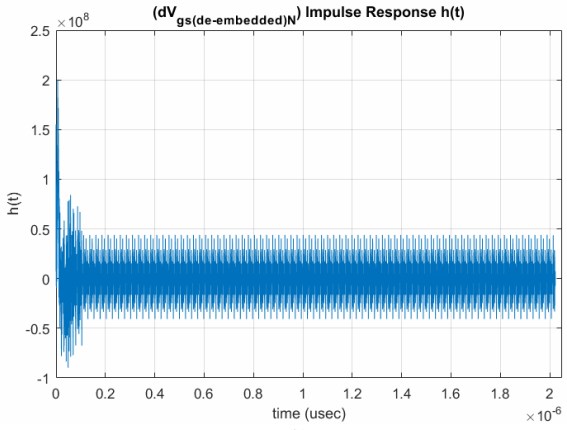

(b)

Fig. 18: (a) step response of Normalized and fitlered, $h_s(t)$ with curve fitting; (b) impulse response h(t))

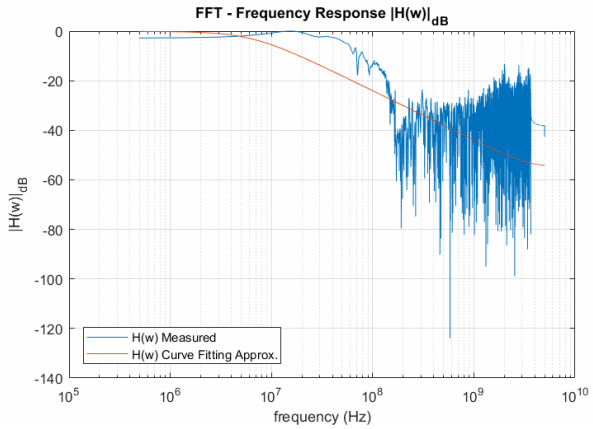

Fig. 19: Multirate sampling-FFT/frequency response H(ω)

Compared to the lumped model with time constant 2.51×10^{-8} sec the response has a slow decaying trend of H(ω) between 10MHz-20MHz., after that it starts to decay rapidly:

The H(ω) computed here is the normalized frequency response of the system and has more than one thermal resistance and capacitance via observation. It is desirable to extract these parameters such that a clearer understanding of

the extraction technique and HEMT devices can be established.

VI. CONCLUSION

In the paper, delta V_{gs} measurement technique is used for measuring channel temperature and extraction of thermal resistance and thermal capacitance. It measures the average channel temperature underneath the gate. The proposed technique provides a quick, easily repeatable and non-destructive determination of thermal parameters. It utilizes the generic laboratory instruments such as oscilloscope and function generator, as compared to other techniques for instance Liquid Crystal Measurement, Photocurrent Spectral Analysis and Micro-Raman Spectroscopy require specialized laboratory instruments which are very expensive and are not easily available. This technique has some limitations as well i.e. oscilloscope adds LSB quantization error while data acquisition system also appends errors in the measurement system. In order to minimize their effects, various optimization methods are applied to remove the LSB quantization error and different types of cables and connectors combinations are used to improve the data acquisition system results.

θ_{th} has been found for three different HEMT devices on the same wafer with almost same dimensions and geometries. The values of θ_{th} are approximately similar for all the three devices with slight variations. Also, the channel temperature variation with respect to change in power dissipation is constant for a particular device. These results ensure that θ_{th} can be measured with considerable precision and accuracy by delta V_{gs} method. The agreement of θ_{th} values for the three devices mounted on the same wafer also verifies the accuracy of our automated measurement test-bench. The test bench still has room for more improvement and can be adopted for other devices such as GaN eHEMT's which are widely popular in power electronics.

REFERENCES

[1] J. Joh, J. A. del Alamo, U. Chowdhury, T. Chou, H. Tserng and J. L. Jimenez, "Measurement of Channel Temperature in GaN High-Electron Mobility Transistors," *IEEE Trans. Electron Devices*, vol. 56, no. 12, pp. 2895-2901, Dec. 2009, doi: 10.1109/TED.2009.2032614.

[2] A. M. Darwish, A. J. Bayba and H. A. Hung, "Accurate determination of thermal resistance of FETs," IEEE Trans. Microw. Theory Techn.,, vol. 53, no. 1, pp. 306-313, Jan. 2005, doi: 10.1109/TMTT.2004.839916.

[3] M. Zhang, W. Che and K. Ma, "A Novel Hybrid Method for Estimating Channel Temperature and Extracting the AlGaN/GaN HEMTs Model Parameters," in IEEE Transactions on Electron Devices, vol. 65, no. 4, pp. 1340-1347, April 2018, doi: 10.1109/TED.2018.2808267.

[4] X. Chen, S. Boumaiza and L. Wei, "Self-Heating and Equivalent Channel Temperature in Short Gate Length GaN HEMTs," in IEEE Transactions on Electron Devices, vol. 66, no. 9, pp. 3748-3755, Sept. 2019, doi: 10.1109/TED.2019.2926742.

[5] B. M. Tenbroek, M. S. L. Lee, W. Redman-White, J. T. Bunyan and M. J. Uren, "Self-heating effects in SOI MOSFETs and their measurement by small signal conductance techniques," *IEEE Trans. Electron Devices*, vol. 43, no. 12, pp. 2240-2248, Dec. 1996, doi: 10.1109/16.544417.

[6] S. Nuttinck et al., "Thermal analysis of AlGaN-GaN power HFETs," IEEE Trans. Microw. Theory Techn.,, vol. 51, no. 12, pp. 2445-2452, Dec. 2003, doi: 10.1109/TMTT.2003.819192.

[7] B. González, B. Aja, E. Artal, A. Lázaro and A. Núñez, "Temperature-Dependent Thermal Capacitance Characterization for SOI-MOSFETs," *IEEE Trans. Electron Devices*, vol. 66, no. 10, pp. 4120-4125, Oct. 2019

[8] Z. Qiu, J. Zhang, P. Ning and X. Wen, "Reliability modeling and analysis of SiC MOSFET power modules," IECON 2017 - 43rd Annual Conference of the IEEE Industrial Electronics Society, Beijing, 2017, pp. 1459-1463, doi: 10.1109/IECON.2017.8216248.

[9] J. A. Mittereder, J. A. Roussos, W. T. Anderson and D. E. Ioannou, "Quantitative measurement of channel temperature of GaAs devices for reliable life-time prediction," *IEEE Trans. Reliability*, vol. 51, no. 4, pp. 482-485, Dec. 2002. doi: 10.1109/TR.2002.804487

[10] A. M. Darwish, A. J. Bayba and H. A. Hung, "Thermal resistance calculation of AlGaN-GaN devices," IEEE Trans. Microw. Theory Techn.,, vol. 52, no. 11, pp. 2611-2620, Nov. 2004, doi: 10.1109/TMTT.2004.837200.

[11] V. Smirnov, V. Sergeev, A. Gavrikov and A. Kulikov, "Measuring Thermal Resistance of GaN HEMTs Using Modulation Method," in IEEE Transactions on Electron Devices, vol. 67, no. 10, pp. 4112-4117, Oct. 2020, doi: 10.1109/TED.2020.3013509.

[12] A. Azuma, T. Asamura, Y. Toyoshima and M. Kakumu, "Precise measurement method of source and drain parasitic resistance and design guideline for scaled MOSFET," Proceedings of 1994 VLSI Technology Symposium, Honolulu, HI, USA, 1994, pp. 129-130, doi: 10.1109/VLSIT.1994.324423.

[13] Jong-Wook Lee and K. J. Webb, "A temperature-dependent nonlinear analytic model for AlGaN-GaN HEMTs on SiC", IEEE Trans. Microw. Theory Techn.,, vol. 52, no. 1, pp. 2-9, Jan. 2004, doi: 10.1109/TMTT.2003.821227.

[14] J. H. Park and C. C. Lee, "A new configuration of nematic liquid crystal thermography with applications to GaN-based devices," IEEE Trans. Instrum. Meas., vol. 55, no. 1, pp. 273–279, Feb. 2006.

[15] Andrea Reale, Aldo Di Carlo, Marco Peroni, Claudio Lanzieri, and S. Lavagna, "Thermal Maps of GaAs P-HEMT: A Novel System Based on the Photocurrent Spectral Analysis" *IEEE Trans. Electron Devices*,, Vol. 54, No. 4, April 2007.

[16] A. Sarua, H. Ji, M. Kuball, M. J. Uren, T. Martin, K. P. Hilton, et al., "Integrated micro-Raman/infrared thermography probe for monitoring of self-heating in AlGaN/GaN transistor structures," *IEEE Trans. Electron Devices*, vol. 53, pp. 2438-2447, 2006.

[17] A. Sarua, H. Ji, M. Kuball, M. J. Uren, T. Martin, K. P. Hilton, and R. S. Balmer, "Integrated micro-Raman/infrared thermography probe for monitoring self-heating in AlGaN/GaN transistor structures," *IEEE Trans. Electron Devices*, vol. 53, no. 10, pp. 2438–2447, Oct. 2006.

[18] H. Fukui, "Thermal resistance of GaAs field-effect transistors," in *IEDM Tech. Dig.*, 1980, pp. 118–121.

[19] I. Ahamd, V. Kasisomayajula, M. Holtz, J. M. Berg, S. R. Kurtz, C. P. Tigges, A. A. Allerman, and A. G. Baca, "Self-heating study of an AlGaN/GaN-based heterostructure field-effect transistor using ultraviolet micro-Raman scattering," *Appl. Phys. Lett.*, vol. 86, no. 17, p. 173 503, Apr. 2005

[20] M. Wu et al., "Accurate Measurement of Channel Temperature for AlGaN/GaN HEMTs," *IEEE Trans. Electron Devices*, vol. 65, no. 11, pp. 4792-4799, Nov. 2018. doi: 10.1109/TED.2018.2868807

[21] M. Z. Wang et al., "Electrically measuring the peak channel temperature of power GaAs MESFET," [1993 Proceedings] Ninth Annual IEEE Semiconductor Thermal Measurement and Management Symposium, Austin, TX, USA, 1993, pp. 112-116, doi: 10.1109/STHERM.1993.225324.

[22] P.D. Maycock, "Thermal conductivity of silicon, germanium, III–V compounds and III–V alloys," Solid-State Electronics, Volume 10, Issue 3, 1967, Pages 161-168. doi: 10.1016/0038-1101(67)90069-X.

[23] H. Fukui, "Thermal resistance of GaAs field-effect transistors," 1980 International Electron Devices Meeting, Washington, DC, USA, 1980, pp. 118-121, doi: 10.1109/IEDM.1980.189768.

[24] L. Yang, Z. Chen, X. Xu and J. Zhang, "Study on the Heat Transfer of GaN-Based High Power HEMTs," in *IEEE Transactions on Semiconductor Manufacturing*, vol. 30, no. 4, pp. 526-530, Nov. 2017, doi: 10.1109/TSM.2017.2739134.

[25] Current Feedback Amplifier LT1210 Data Sheet - Linear Technology.Link: https://www.analog.com/media/en/technical-documentation/data-sheets/lt1210.pdf

[26] Link: https://www.nitronics.co.uk/

[27] Alan Woodsworth, "Fundamentals of Fast Pulsed IV Measurements", Agilent Technologies 2014. https://www.keysight.com/upload/cmc_upload/All/9Feb14Slides.pdf

[28] Robert Anholt, "Electrical and Thermal characterization of MESFETs, HEMTs and HBTs", Artech House Boston London, 1995.

[29] R. Menozzi *et al*., "Temperature-Dependent Characterization of AlGaN/GaN HEMTs: Thermal and Source/Drain Resistances," in *IEEE Transactions on Device and Materials Reliability*, vol. 8, no. 2, pp. 255-264, June 2008, doi: 10.1109/TDMR.2008.918960.

[30] J. P. Deyst, T. M. Souders and J. J. Blair, "Uncertainties of frequency response estimates derived from responses to uncertain step-like inputs," Quality Measurement: The Indispensable Bridge between Theory and Reality (No Measurements? No Science! Joint Conference - 1996: IEEE Instrumentation and Measurement Technology Conference and IMEKO Tec, Brussels, Belgium, 1996, pp. 151-155 vol.1, doi: 10.1109/IMTC.1996.507366.

[31] M. Saeki and K. Saito, "Estimation of frequency response set from interval data of step response," *Proceedings of the 41st SICE Annual Conference. SICE 2002.*, Osaka, 2002, pp. 1233-1236 vol.2, doi: 10.1109/SICE.2002.1195361.